Nanoscale electronic inhomogeneities in $1T$-TaS$_2$

B. Campbell [1,*] J. V. Riffle,[1,*] A. de la Torre [2,†] Q. Wang [2] K. W. Plumb [2] and S. M. Hollen [1,‡]

^{1}*Department of Physics and Astronomy, University of New Hampshire, Durham, NH 03824, USA*
^{2}*Department of Physics, Brown University, Providence, RI, 02912, USA*

We report a set of scanning tunneling microscopy (STM) and spectroscopy (STS) experiments studying native defects in CVT grown $1T$-TaS$_2$. Six different sample surfaces from four bulk crystals were investigated. Wide area imaging reveals a prevalence of nanometer-scale electronic inhomogeneities due to native defects, with pristine regions interspersed. These inhomogeneities appear in typical as-grown crystals and coexist with a well-formed commensurate charge density wave of $1T$-TaS$_2$ at low temperatures. Electronic inhomogeneities show up both as variations in the apparent height in STM and in the local density of states in STS; the bands can shift by 60 meV and the gap varies by more than 100 meV across inhomogeneities. These inhomogeneities are present in similar concentration across large-scale areas of all samples studied, but do not influence the charge density wave formation on local or global scales. The commensurate charge density wave exhibits long-range order and remains locally intact in the presence of these inhomogeneities.

I. INTRODUCTION

Lattice defects can greatly affect the structural, optical, and electronic properties of materials and have an increased impact in the 2D limit, where much materials and device development is now focused. Of the dichalcogenides, $1T$-TaS$_2$ is an exciting material because of its rich phase diagram, complex examples of unusual phenomena, and potential applications in memory and ultrafast switching devices [1–6]. The many reports describing observations of and theoretical explanations for unusual behavior in $1T$-TaS$_2$—including Mott physics, quantum spin liquid behavior [7], memristive switching [3,6], hidden and metastable phases [8,9], and topological and chiral charge density waves [10,11]—demonstrate its complexity and the level of interest from the condensed matter community. An important but often overlooked point in this discussion is the impact of native defects on the properties of $1T$-TaS$_2$. Induced defects were shown to suppress the commensurate CDW phase and insulating ground state and induce superconductivity at 2.5 K in one example [12], and in another, K dopants did not affect the CDW order, but did induce metallicity [13]. On the other hand, little attention has been paid to intrinsic defects. A recent study reported the local electronic structure of intrinsic defects by STM, characterized five distinct defects by local density of states measurements, and made partial assignment of these defects using density functional theory calculations [14].

We report a set of low-temperature scanning tunneling microscopy (STM) experiments over large areas of $1T$-TaS$_2$ that reveal the existence of nanometer-scale electronic inhomogeneities in addition to the commonly observed commensurate charge density wave (C-CDW). We surveyed six different sample surfaces from four bulk crystals, and investigated large areas of each sample. The inhomogeneities are observed as variations in the apparent height in STM topographs and the local density of states (LDOS) measured by scanning tunneling spectroscopy (STS). STS shows that the band edges shift by up to 60 mV across these features, and the gap is suppressed near their center. Atomic resolution images support that lattice defects are a source of electronic inhomogeneity. While the local CDW amplitude is reduced by the electronic inhomogeneity, we find that the defects or the associated electronic inhomogeneities do not modify the period and phase of the C-CDW. Since the bulk features of these samples, including the resistivity versus temperature and the observation of the C-CDW by XRD, are in line with broadly accepted results from the literature, the coexistence of nanoscale inhomogeneities with the C-CDW demonstrates the importance of real space images of $1T$-TaS$_2$ and similar materials, and could potentially contribute to understanding their perplexing behavior.

II. EXPERIMENTAL DETAILS

Single crystals of $1T$-TaS$_2$ were grown from stoichiometric amounts of elemental Ta and S by chemical vapor transport, using iodine as a transport agent. Starting materials were sealed in quartz tubes and heated in a three zone furnace under a $950°$C–$850°$C temperature gradient for 240 h, and then quenched in ice water to stabilize the $1T$ phase.

To perform the STM experiments, a bulk $1T$-TaS$_2$ crystal was mounted onto a stainless steel STM sample plate using conductive, UHV-safe epoxy, then introduced into the ultra-high vacuum chamber. Using a cleaving screw and carbon

---

*These authors contributed equally.

†Present address: Department of Physics, Northeastern University, Boston, MA 02115.

‡shawna.hollen@unh.edu

tape, the surface of the TaS$_2$ crystal was cleaved at room temperature and $\sim 10^{-10}$ torr. The sample was then studied using our RHK Technology PanScan Freedom, closed-cycle STM, with an operating temperature of 10 K. Pt-Ir cut tips were used in all the experiments reported here. Images were analyzed with WSxM [15] and custom python codes are available on github [16]. Determination of the band gap for each STS spectrum was done by identifying at least six contiguous dI/dV measurements that were within 0.25 pS of zero. The gap width was then defined as the voltage range of this contiguous set, and the gap center was defined as the average of the end points of this contiguous set. The tolerance of 0.25 pS was fine tuned by visual inspection of the resulting gaps plotted over their respective LDOS curve. X-ray diffraction measurements were performed on a four circle diffractometer at Brown University using a microfocused Ag Kα x-ray source and a GaAs area detector (256 × 256 pixels) with 55 × 55 µm^2 pixel size situated 96 cm away from the center of rotation.

III. EXPERIMENTAL RESULTS

Samples of 1T-TaS$_2$ were grown by a standard chemical vapor transport (see experimental details) and cleaved in ultrahigh vacuum at room temperature. Bulk resistivity measurements of as-grown crystals match expectations from literature and temperature dependent x-ray diffraction reveals well formed charge-density waves exhibiting a nearly commensurate to commensurate transition at 190 K and significant thermal hysteresis consistent with literature [17,18]. Large area STM and STS surveys at 10 K revealed significant populations of defects (approximate density of 300 per million atoms) and signatures of electronic disorder, with pristine regions interspersed. Figure 1 presents images of two different samples from these experiments. Figure 1(a) shows an STM topographic image of a pristine region of a 1T-TaS$_2$ sample with uniform contrast while Fig. 1(c) shows a similar image from a region with nanometer-scale inhomogeneities. Figure 1(a) is more similar to typically reported STM images. It shows bright features in a triangular lattice with a periodicity of 1.2 nm arising from the commensurate charge density wave (C-CDW), and it shows the atomic lattice of the surface S atoms (see overlay in inset). The C-CDW in STM topographs is primarily an electronic feature with an apparent height that corresponds to the integrated local density of states between the tip-sample bias and the Fermi energy. It is commensurate with the atomic lattice, forming a $\sqrt{13} \times \sqrt{13}$ superstructure rotated 13.9° from the lattice vectors [17–19]. In order to extract the C-CDW wave vector, we compute the fast-Fourier transform (FFT) of the topographic image [Fig. 1(b)]. By comparing the magnitude and direction of the q vector for the CDW (inner peaks, red arrow) and the atomic lattice (outer peaks, blue arrow), we extract a C-CDW wave vector that is consistent with the expected values for the C-CDW.

Figures 1(c) and 1(d) show the same type of data as Fig. 1(a) and 1(b), but for a region with inhomogeneities. The C-CDW and atomic lattice are both resolved and the FFT compares well with 1(b), showing both the atomic lattice and the CDW. There are differences between these images that can be attributed to the tip termination. For example, the atomic lattice in Fig. 1(c) is clearly resolved, but the charge
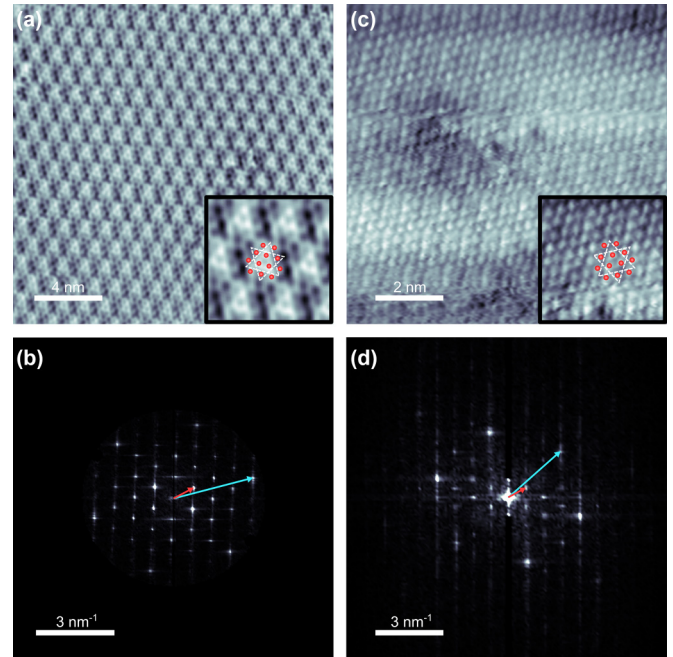

FIG. 1. STM topographs of the 1T-TaS$_2$ surface at $T = 10$ K after cleaving in ultrahigh vacuum. (a), (c) Topography showing the C-CDW and atomic resolution [(a) 500 mV, 150 pA; (b) 550 mV, 145 pA]. Insets: magnified view showing resolution of S atoms with lattice overlay (red dots) and star of David C-CDW pattern (dashed white triangles). (b), (d) Fast-Fourier transform (FFT) of images in (a), (c). Blue vector corresponds to q_{lattice} and red vector to q_{CDW}. $|q_{\text{CDW}}| = 0.853 \pm 0.03$ nm^{-1} (0.27 ± 0.12 rlu) for (b), $|q_{\text{CDW}}| = 0.912 \pm 0.11$ nm^{-1} (0.31 ± 0.25 rlu) for (d).

density wave is much more subtle than in 1(a) [see star of David in Fig. 1(c) inset]. The background contrast in 1(c) is not uniform, and this nonuniformity is present for a wide range of imaging parameters. There is a dark region left of the center, roughly 5 nm across, and another in the upper right corner. These features create a diffuse signal centered on zero in the FFT [1(d)]. Figure S1 shows a representative set of images that all show a clear C-CDW with an inhomogeneous background from four different surfaces from three different bulk crystals [20]. Figure 1(a), is a region of Fig. S1(a) that is free of defects.

Large area images, like the 70 nm wide region in Fig. 2, show that inhomogeneities are distributed over the entire surface and that the C-CDW maintains its coherence on a length scale much larger than the average separation between defect sites. To illustrate this, we separated the nanoscale disorder from the C-CDW in Fig. 2(a) using a cutoff filter on the FFT [Fig. 2(a), inset]. Figure 2(b) shows the low-frequency nanoscale inhomogeneities, with an average nearest neighbor separation of $L_D \approx 3.5$ nm. Figure 2(c) shows the isolated C-CDW. The C-CDW is uninterrupted over the imaging area, with no phase slips, discontinuities, or domains. A linecut of the unfiltered image in Fig. 2(d) shows the apparent height of the C-CDW with a 1.2 nm periodicity combined with the nonperiodic modulations in amplitude that are due to the 5–10 nm-diameter inhomogeneities.
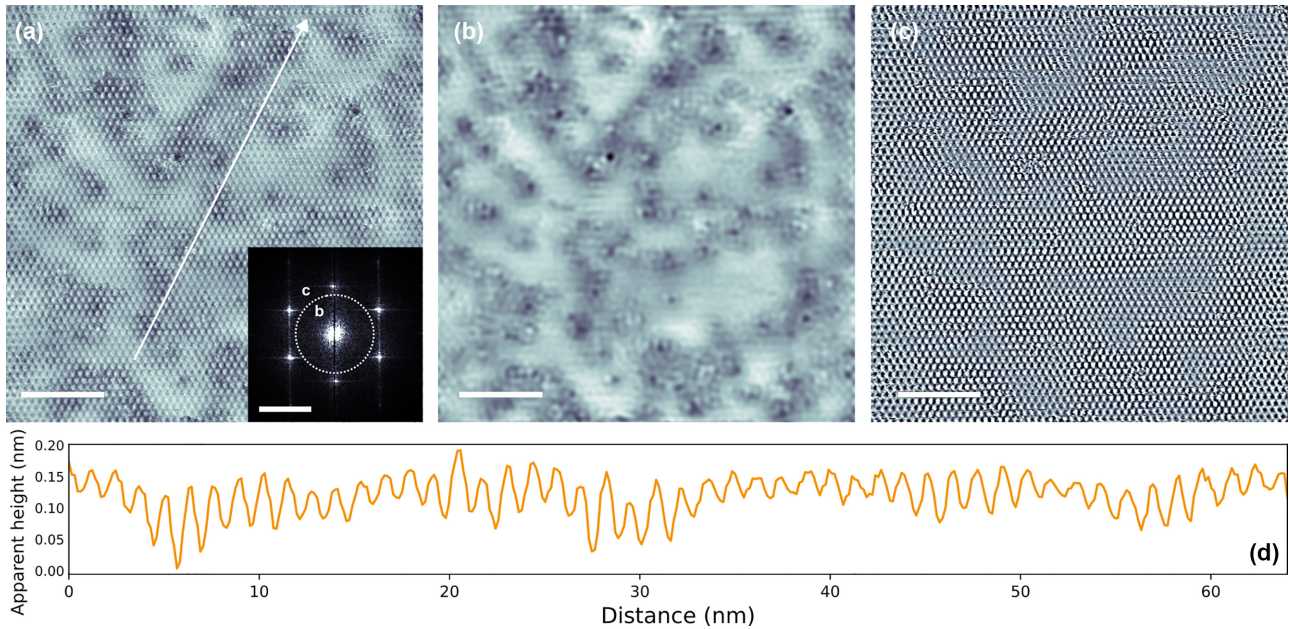
FIG. 2. (a) Large area STM topograph showing the C-CDW and apparent height variations (300 mV, 65 pA setpoint). Scale bar is 14 nm. Color range is from 0 nm (black) to 2.92 nm (white). Inset: fast-Fourier transform. FFT scale bar is 1.5 nm^{-1}. (b) Topograph with low-pass filter applied, as indicated by the dashed circle in (a) inset, to bring out the nanoscale apparent height modulations. Color range is from 0 nm to 0.236 nm. (c) Topograph with high pass filter applied, as indicated by the dashed circle in (a) inset, to show the uninterrupted C-CDW. Color range is from 0.1 nm to 0.193 nm. (d) Line cut over white arrow in (a) showing the 1.2 nm periodic modulations of the C-CDW and the additional large-scale structure and amplitude variations created by the larger-scale electronic disorder.

The coherence length of the C-CDW is not measured well in the real-space images we acquired since they represent local information only and have a limited size. Figure 3 shows XRD data at $T = 80$ K on an identically prepared $1T$-TaS$_2$ sample. We extract an average C-CDW correlation length of $\xi_{CDW} = 35 \pm 5$ nm from the full-width half maximum of a transverse scan through the satellite C-CDW peaks (dotted orange line). From these data we conclude $\xi_{CDW} \gg L_D$.

To gain more insight into the source of these inhomogeneities, we examine atomically resolved images, like those in Fig. 4. Here we see the atomic lattice appears to be disrupted near several bright and dark features, as indicated by red arrows in the figure. Based on these and similar images, we assign the source of the inhomogeneities to lattice defects,

most likely vacancies and substitutions. There are also regions in Fig. 4 that show contrast in the apparent height, but no obvious disruption to the surface atoms (dashed yellow circles). These features appear larger by a factor of ≈ 1.5–2 across and are less pronounced than those associated with surface defects. Larger scale images (Fig. 2) also show nanometer-scale features with a range of apparent heights and lateral sizes. These observations are all consistent with defects imaged in multiple crystalline layers below the surface, a common occurrence in STM imaging of semiconductors [21–23]. Thus, defects that cause the nanoscale electronic inhomogeneities are not limited to the surface layer (so are not a product of the cleave), and are likely evenly distributed throughout the bulk crystal. We estimate the defect density by counting the
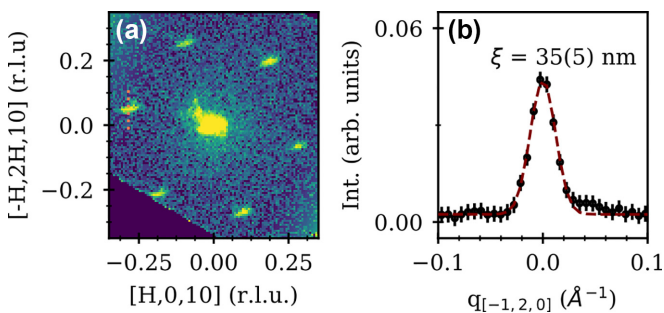

FIG. 3. (a) Reciprocal space map perpendicular to $[0, 0, L]$ centered at $L = 10$ (integration range $\delta L \pm = .04$ r.l.u.). The six satellite peaks correspond to the C-CDW at $T = 80$ K. (b) Transverse cut through a representative C-CDW peak as indicated by the orange dashed line in (a). Dotted red line encodes a Gaussian fit to the data.
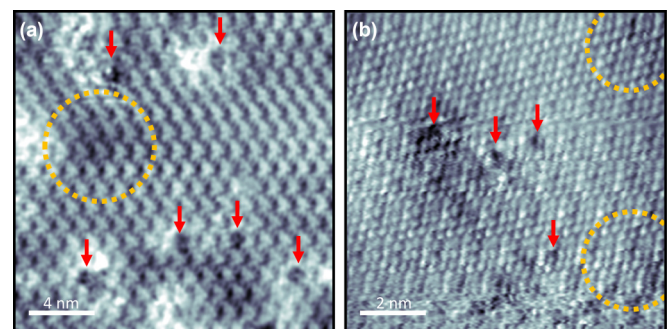

FIG. 4. STM topographs showing the C-CDW and defective atomic lattice. (a) -500 mV and 50 pA, and (b) 550 mV and 145 pA. Red arrows indicated regions where the atomic lattice appears disrupted. Dashed yellow circles highlight regions with diffuse apparent height differences, but no lattice disruption.
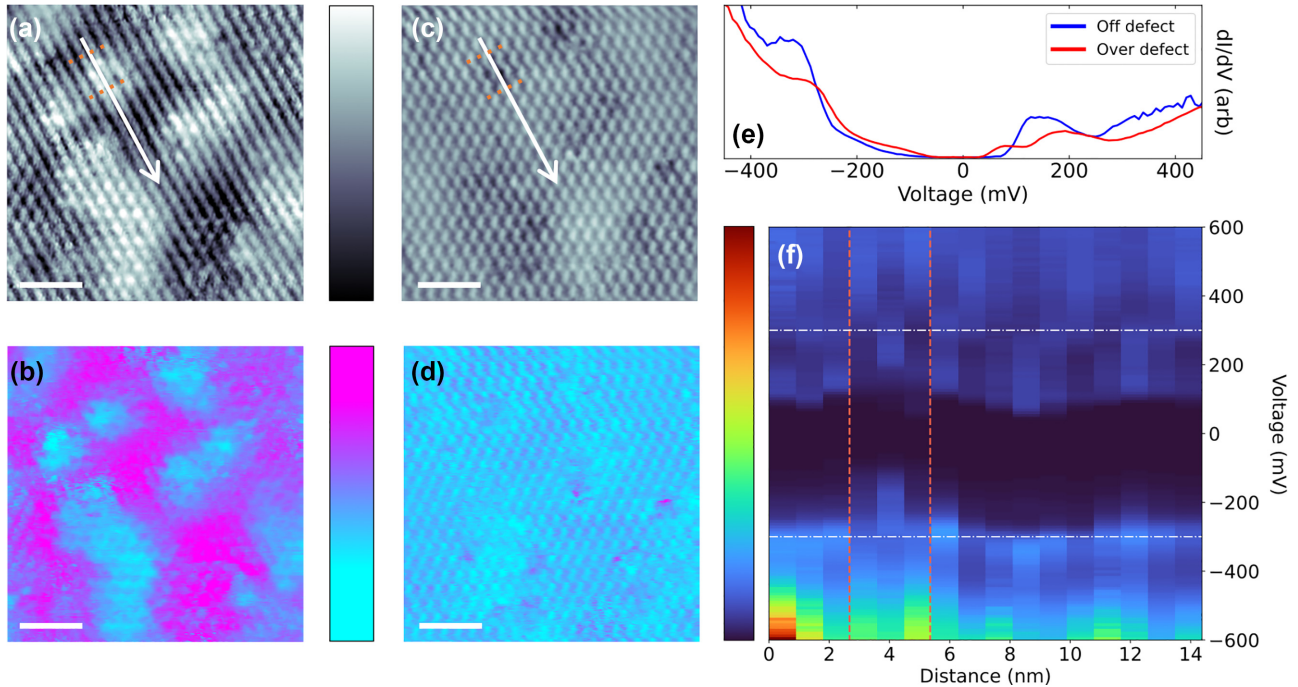
FIG. 5. (a), (c) STM topographs and (b), (d) dI/dV maps taken at -300 mV and 300 mV, respectively. Scale bar is 5 nm. (e) dI/dV spectroscopy taken on and off the defect between the orange dashed lines in a and c. (f) dI/dV point spectroscopy taken over the white line marked in a and c. Orange, dashed lines denote the boundary of the defect and the x-axis denotes distance along the cut, increasing in the direction of the arrow in a, c. The horizontal, white lines denote slices at ±300 mV that correspond to the dI/dV maps in (b), (d).

number of defects in a large-scale image (108 in Fig. 2) and comparing this number to the number of atoms in three layers of TaS_2 (with 31.2 atoms/nm^2 in each layer), which gives 235 ppm (108 defects in 459 000 atoms), or equivalently 0.07% "doping" (per unit cell). This is potentially an underestimate by a factor of ~ 2 because it is not easy to determine from the data how many layers below the surface we are imaging, and three layers may be an overestimate.

The defects strongly impact the crystal's local electronic structure, which we illuminate with measurements of the local density of states (LDOS). First, by comparing topography at negative bias [filled states, Fig. 5(a)] and positive bias [empty states, Fig. 5(c)]. We observe a strong voltage dependence of the apparent height, which indicates significant variation in the LDOS. We directly probed the LDOS using both dI/dV spatial mapping at set biases [Figs. 5(b) amd 5(d)] and location-dependent spectroscopy [Figs. 5(e) and 5(f)]. The spatial features of the LDOS in Figs. 5(b) and 5(d) mirror those in the topography, Figs. 5(a) and 5(c). At the chosen positive bias, the LDOS variations are weaker and more localized [Fig. 5(d)] than those at the chosen negative bias [Fig. 5(b)].

dI/dV point and line spectroscopy in Figs. 5(e) and 5(f) show the typical shape of the LDOS on $1T$-TaS_2 in which a ~ 300 mV gap is bounded by two peaks, which are usually assigned to the upper and lower Hubbard bands of the Mott gap [24,25]. Here, we observe spatial shifts in the energy of the peaks and the gap edges of up to ~ 60 mV. The relative contrast of the LDOS in Figs. 5(b) and 5(d) is also made clear since -300 mV [bottom dashed line in 5(f)] cuts across the strong variations in the lower Hubbard band while $+300$ mV

corresponds to an energy deeper in the conduction band, beyond the upper Hubbard band. Notably, the gap is suppressed over the defect in (a) and (c) [Fig. 5(e)]. The combination of LDOS maps in Figs. 5(b) and 5(d) and the line spectra in Figs. 5(e) and 5(f) show that defects in the TaS_2 create strong electronic inhomogeneities, causing ~ 60 mV variations in the local doping and strong disruptions to the local electronic structure. This observation is reminiscent of behavior in doped Mott insulators, including iridates [26] and cuprates [27,28].

These strong local disruptions result in nanoscale inhomogeneities in the electronic structure over the entire crystal, as shown over a large region in Fig. 6. A 16×16 grid of dI/dV point spectroscopy indicate wide variations in both gap width and shifting of the gap center across a 100×100 nm^2 area. The mean dI/dV spectra is shown in 6(b) as the solid blue LDOS curve with the standard deviation indicated by the shaded region. The central red, vertical line shows the average gap center, and the red arrows indicate the average gap width. We chose to define the gap width using a threshold above $dI/dV = 0$ (see experimental details) so that it is independent of the upper and lower Hubbard peak locations. It should be noted that this choice does underestimate the gap width compared to the more typical choice that measures the separation of the Hubbard peaks. Figure 6(c) shows the spatial variations in gap width over the region in (a); the average gap width is 120 mV and the standard deviation of the set of gap widths is 50 mV. The gap center in Fig. 6(d) also shows large shifts, up to 60 mV positive and negative. Over a large scale, the shifts tend to cancel, leading to an average shift close to zero [as indicated in Fig. 6(b)].
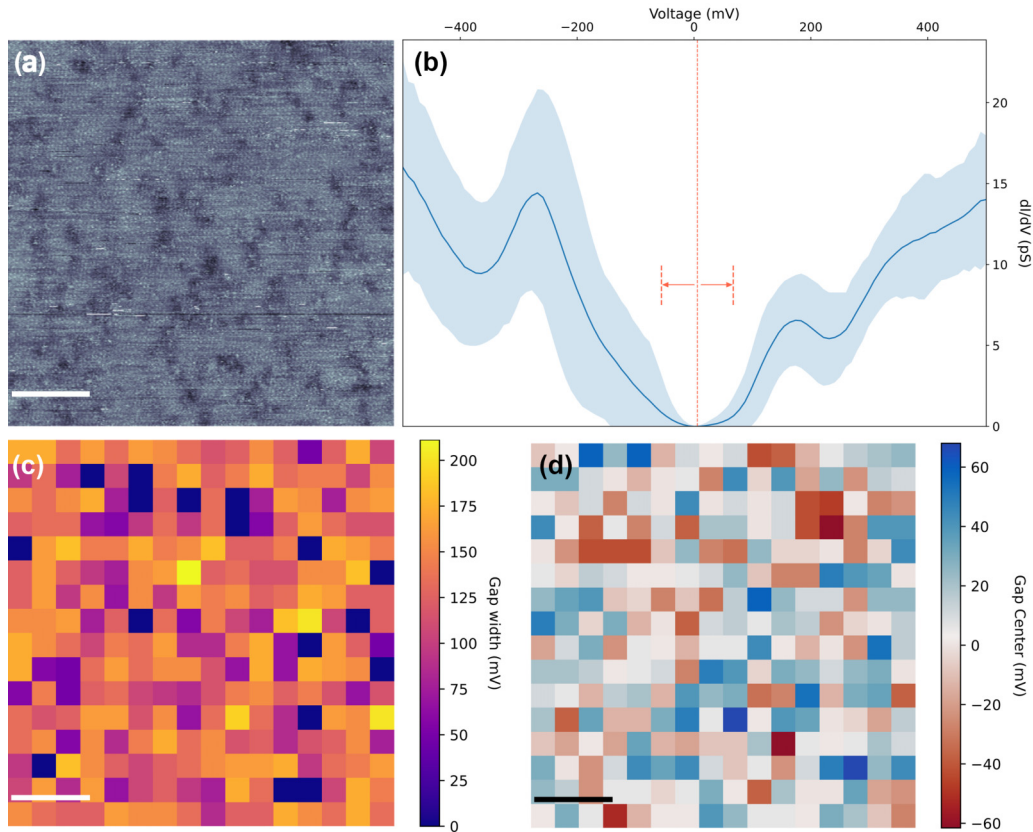
FIG. 6. 16×16 grid of STS measurements over a 100×100 nm^2 area showing nanometer-scale inhomogeneities in gap width and gap center. (a) TM topograph showing the nanometer-scale disorder. (b) Mean LDOS taken over all 16×16 spectra plotted in blue with standard deviation denoted by the shaded region. The mean gap center is marked by the red vertical, dashed line and the mean gap width is indicated by the red arrows. Mean gap width is 120 ± 50 mV and gap centers show variations up to 60mV. (c) Spatial plot of the gap width as defined in methods. Each pixel represents an STS measurement at the center of a 6.25×6.25 nm^2 section of (a). (d) Spatial plot of the gap center as defined in methods. Red and blue denote a negative and positive shift, respectively. All scale bars are 20 nm.

IV. DISCUSSION

Because of the combined importance of physical and electronic structure, we cannot directly identify the defect types from STM topographs. The defects imaged in Fig. 4 seem to be mostly of the same species, but it is likely that over large areas we are imaging multiple types, including vacancies, substitutions, and possibly intercalants. Recent work by Lutsyk *et al.* [14] identified five distinct defect types in high resolution STM and STS data, one of which they identified as an S vacancy, which are common in dichalcogenides [11,29]. In atomic-resolution images, the sensitivity of the tunneling current to different orbitals depends strongly on the tip termination. Sensitivity of the STM to the outer S atoms has been supported by DFT [14,30] despite the dominance of the Ta d_z orbitals in the wavefunction [31] that would suggest that image contrast would be due primarily to Ta atoms. Because of this prior work, and since the formation energy of S vacancies is low, it is reasonable to attribute the defects we observe to S vacancies. However, Lutsyk *et al.* found the sulfur vacancy, identified by DFT, to have a very localized impact on the LDOS, extending no more than a single CDW site. Another defect, not identified in the DFT calculations but speculated to be a foreign atom substitution, was found to have electronic features extending several nanometers, which

is more consistent with the large-area surveys we present here. Still, this comparison is inconclusive since, in their study, the defect with nanometer-scale electronic imprint still exhibited a clear gap. Overall, these native defects have a strong effect on the electronic structure and yet are not detected by typical "bulk" characterization. We suggest that studies of mesoscale samples or devices consider how these defects may affect their results, and potentially have their samples closely interrogated with STM.

We note that we do not see any signs of strain in our large scale images of these cleaved bulk crystals. Since strain is known to induce CDW domains and even a metallic mosaic phase [32] and topological networks of CDW defects [10], lack of strain is consistent with our single-domain C-CDW observations. When combined with the LDOS measurements, this also makes clear that the nanoscale features are all electronic and do not correspond to bending or wrinkling of the surface.

We would like to emphasize the remarkable robustness of the C-CDW to lattice defects and their associated electronic disorder, when compared to interlayer disorder (e.g., [33]) and moderate lattice strain [10,32]. As described above, the CDW correlation length in 1T-TaS$_2$ is approximately ten times larger than the average defect separation. The insensitivity of

the CDW to lattice defects is apparent in our large-scale STM images (e.g., Fig. 2), XRD measurements (Fig. 3), and low-temperature transport (see the Supplemental Material [20]). A recent study of the impact of disorder on the CDW in ErTe$_3$ found that even 0.3% intercalation of Pd causes some disruption of the CDW order [34], detectable as dislocations in the CDW phase. No CDW dislocations are present in our large-scale STM data despite a similar average separation between defects ($\sim$4 nm) to that observed in ErTe$_3$. On the other hand, the reported changes in the local electronic structure near defects are suggestive of a weak Mott state in 1T-TaS$_2$. While we are not controllably introducing dopants in our sample, assuming each of the point defects donates a single electron, we would expect $\approx 0.07 e^-$ per unit cell with respect to a pristine sample. In cuprates [27,28] and iridates [26], changes in the local electronic density of states are only observed for much larger dopant concentrations ($\approx 2-5\%$) as a result of the stronger carrier localization in these two material families. Indeed, we do not observe any signatures of tip induced band bending expected in lightly doped Mott insulators [35].

The observed dichotomy between the robustness of the microscopic properties of the C-CDW to out-of-plane and in-plane disorder further motivates the development of memristive integrable devices based on few-layers samples of 1T-TaS$_2$ [3–6] and the theoretical study of the impact of the disorder on the correlation length of charge density waves [36–39]. Our results reopen questions of how the disorder affects charge-ordered phases in correlated systems [40,41], and emphasize the importance of real-space measurements in resolving the structural and electronic properties of quantum materials.

V. CONCLUSIONS

The data presented here shows the prevalence and importance of nanoscale inhomogeneities to the local electronic properties of 1T-TaS$_2$ at 10 K. We show evidence that the inhomogeneities originate from lattice defects. These features shift the band edges by up to 60 mV and in some cases the gap is degraded directly over the defect sites. Overall, these data contribute a broad picture of electronic inhomogeneities in 1T-TaS$_2$ and CDW materials which will play an important role in the observations of out-of-equilibrium states and on any electronic device applications, e.g., neuromorphic computing [6], and provides an example of a C-CDW robust to a high level of disorder.

[1] R. Manzke, T. Buslaps, B. Pfalzgraf, M. Skibowski, and O. Anderson, On the phase transitions in 1T-TaS$_2$, Europhys. Lett. **8**, 195 (1989).

[2] Z. Xu, H. Yang, X. Song, Y. Chen, H. Yang, M. Liu, Z. Huang, Q. Zhang, J. Sun, L. Liu, and Y. Wang, Topical review: recent progress of charge density waves in 2D transition metal dichalcogenide-based heterojunctions and their applications, Nanotechnol. **32**, 492001 (2021).

[3] D. Mihailovic, D. Svetin, I. Vaskivskyi, R. Venturini, B. Lipovšek, and A. Mraz, Ultrafast non-thermal and thermal switching in charge configuration memory devices based on 1T-TaS$_2$, Appl. Phys. Lett. **119**, 013106 (2021).

[4] S. R. Bauers, M. B. Tellekamp, D. M. Roberts, B. Hammett, S. Lany, A. J. Ferguson, A. Zakutayev, and S. U. Nanayakkara, Metal chalcogenides for neuromorphic computing: emerging materials and mechanisms, Nanotechnol. **32**, 372001 (2021).

[5] W. Huh, D. Lee, and C.-H. Lee, Memristors based on 2D materials as an artificial synapse for neuromorphic electronics, Adv. Mater. **32** (2020).

[6] M. Yoshida, R. Suzuki, Y. Zhang, M. Nakano, and Y. Iwasa, Memristive phase switching in two-dimensional 1T-TaS$_2$ crystals, Sci. Adv. **1**, e1500606 (2015).

[7] K. T. Law and P. A. Lee, 1T-TaS$_2$ as a quantum spin liquid, Proc. Natl. Acad. Sci. USA **114**, 6996 (2017).

[8] L. Stojchevska, I. Vaskivskyi, T. Mertelj, P. Kusar, D. Svetin, S. Brazovskii, and D. Mihailovic, Ultrafast switching to a stable hidden quantum state in an electronic crystal, Science **344**, 177 (2014).

[9] I. Vaskivskyi, J. Gospodaric, S. Brazovskii, D. Svetin, P. Sutar, E. Goreshnik, I. A. Mihailovic, T. Mertelj, and D. Mihailovic, Controlling the metal-to-insulator relaxation of the metastable hidden quantum state in 1T-TaS$_2$, Sci. Adv. **1**, e1500168 (2015).

[10] J. Ravnik, I. Vaskivskyi, Y. Gerasimenko, M. Diego, J. Vodeb, V. Kabanov, and D. D. Mihailovic, Strain-induced metastable topological networks in laser-fabricated TaS$_2$ polytype heterostructures for nanoscale devices, ACS Appl. Nano Mater. **2**, 3743 (2019).

[11] N. Gao, X. Liang, J. Zhao, and Y. Chen, First-principles study of the atomic structures and catalytic properties of monolayer TaS$_2$ with intrinsic defects, J. Phys. Chem. C **125**, 10362 (2021).

[12] L. J. Li, W. J. Lu, Y. Liu, Z. Qu, L. S. Ling, and Y. P. Sun, Influence of defects on charge–density–wave and superconductivity in 1T-TaS$_2$ and 2H-TaS$_2$ systems, Physica C: Supercond. **492**, 64 (2013).

[13] X. Y. Zhu, S. Wang, Z. Y. Jia, L. Zhu, Q. Y. Li, W. M. Zhao, C. L. Xue, Y. J. Xu, Z. Ma, J. Wen, S. L. Yu, J. X. Li, and S. C. Li, Realization of a metallic state in 1T-TaS$_2$ with persisting long-range order of a charge density wave, Phys. Rev. Lett. **123**, 206405 (2019).

[14] I. Lutsyk, K. Szalowski, P. Krukowski, P. Dabrowski, M. Rogala, W. Kozlowski, M. L. Ster, M. Piskorski, D. A. Kowalczyk, W. Rys, R. Dunal, A. Nadolska, K. Toczek, P. Przybysz, E. Lacinska, J. Binder, A. Wysmolek, N. Olszowska, J. J. Kolodziej, M. Gmitra *et al.*, Influence of structural defects

on charge density waves in $1T$-TaS$_2$, Nano Res. **16**, 11528 (2023).

[15] I. Horcas, R. Fernández, J. M. Gómez-Rodríguez, J. Colchero, J. Gómez-Herrero, and A. M. Baro, WSXM: A software for scanning probe microscopy and a tool for nanotechnology, Rev. Sci. Instrum. **78**, 013705 (2007).

[16] B. Campbell, Analysis for defect induced electronic inhomogeneities in TaS2 paper, https://github.com/bhc1010/Defect-induced-electronic-inhomogeneities-in-TaS2.

[17] P. Fazekas and E. Tosatti, Electrical, structural and magnetic properties of pure and doped $1T$-TaS$_2$, Philos. Mag. B **39**, 229 (1979).

[18] P. Fazekas and E. Tosatti, Charge carrier localization in pure and doped $1T$-TaS$_2$, Physica B+C **99**, 183 (1980).

[19] J. A. Wilson, F. J. D. Salvo, and S. Mahajan, Charge-density waves and superlattices in the metallic layered transition metal dichalcogenides, Adv. Phys. **24**, 117 (1975).

[20] See Supplemental Material at http://link.aps.org/supplemental/10.1103/PhysRevMaterials.8.034002 for representative STM images from other samples and resistivity versus temperature data.

[21] R. M. Feenstra, J. M. Woodall, and G. D. Pettit, Observation of bulk defects by scanning tunneling microscopy and spectroscopy: Arsenic antisite defects in GaAs, Phys. Rev. Lett. **71**, 1176 (1993).

[22] P. Ebert, Nano-scale properties of defects in compound semiconductor surfaces, Surf. Sci. Rep. **33**, 121 (1999).

[23] D. Wong, J. Velasco Jr, L. Ju, J. Lee, S. Kahn, H.-Z. Tsai, C. Germany, T. Taniguchi, K. Watanabe, A. Zettl *et al.*, Characterization and manipulation of individual defects in insulating hexagonal boron nitride using scanning tunnelling microscopy, Nat. Nanotechnol. **10**, 949 (2015).

[24] J.-J. Kim, W. Yamaguchi, T. Hasegawa, and K. Kitazawa, Observation of mott localization gap using low temperature scanning tunneling spectroscopy in commensurate $1T$-TaS$_2$, Phys. Rev. Lett. **73**, 2103 (1994).

[25] D. Cho, Y.-H. Cho, S.-W. Cheong, K.-S. Kim, and H. W. Yeom, Interplay of electron-electron and electron-phonon interactions in the low-temperature phase of $1T$-TaS$_2$, Phys. Rev. B **92**, 085132 (2015).

[26] I. Battisti, K. M. Bastiaans, V. Fedoseev, A. de la Torre, N. Iliopoulos, A. Tamai, E. C. Hunter, R. S. Perry, J. Zaanen, F. Baumberger, and M. P. Allan, Universality of pseudogap and emergent order in lightly doped mott insulators, Nat. Phys. **13**, 21 (2017).

[27] Y. Kohsaka, K. Iwaya, S. Satow, T. Hanaguri, M. Azuma, M. Takano, and H. Takagi, Imaging nanoscale electronic inhomogeneity in the lightly doped mott insulator Ca$_{2-x}$Na$_x$CuO$_2$Cl$_2$, Phys. Rev. Lett. **93**, 097004 (2004).

[28] P. Cai, W. Ruan, Y. Peng, C. Ye, X. Li, Z. Hao, X. Zhou, D.-H. Lee, and Y. Wang, Visualizing the evolution from the mott insulator to a charge-ordered insulator in lightly doped cuprates, Nat. Phys. **12**, 1047 (2016).

[29] Q. Liang, Q. Zhang, X. Zhao, M. Liu, and A. T. S. Wee, Defect engineering of two-dimensional transition-metal dichalcogenides: Applications, challenges, and opportunities, ACS Nano **15**, 2165 (2021).

[30] S. Qiao, X. Li, N. Wang, W. Ruan, C. Ye, P. Cai, Z. Hao, H. Yao, X. Chen, J. Wu, Y. Wang, and Z. Liu, Mottness collapse in 1T$-$TaS$_{2-x}$Se$_x$ transition-metal dichalcogenide: An interplay between localized and itinerant orbitals, Phys. Rev. X **7**, 041054 (2017).

[31] S. W. Hla, V. Marinković, A. Prodan, and I. Muševič, STM/AFM investigations of β-MoTe$_2$, α-MoTe$_2$ and WTe$_2$, Surf. Sci. **352-354**, 105 (1996).

[32] K. Bu, W. Zhang, Y. Fei, Z. Wu, Y. Zheng, J. Gao, X. Luo, Y.-P. Sun, and Y. Yin, Possible strain induced Mott gap collapse in $1T$-TaS$_2$, Commun. Phys. **2**, 146 (2019).

[33] S.-H. Lee, J. S. Goh, and D. Cho, Origin of the insulating phase and first-order metal-insulator transition in $1T$-TaS$_2$, Phys. Rev. Lett. **122**, 106404 (2019).

[34] A. Fang, J. A. W. Straquadine, I. R. Fisher, S. A. Kivelson, and A. Kapitulnik, Disorder-induced suppression of charge density wave order: STM study of Pd-intercalated ErTe$_3$, Phys. Rev. B **100**, 235446 (2019).

[35] I. Battisti, V. Fedoseev, K. M. Bastiaans, A. de la Torre, R. S. Perry, F. Baumberger, and M. P. Allan, Poor electronic screening in lightly doped mott insulators observed with scanning tunneling microscopy, Phys. Rev. B **95**, 235141 (2017).

[36] D. Subires, A. Korshunov, A. H. Said, L. Sánchez, B. R. Ortiz, S. D. Wilson, A. Bosak, and S. Blanco-Canosa, Order-disorder charge density wave instability in the kagome metal (Cs, Rb)V$_3$Sb$_5$, Nat. Commun. **14**, 1015 (2023).

[37] M. Corasaniti, R. Yang, L. Degiorgi, J. A. W. Straquadine, A. Kapitulnik, and I. R. Fisher, Impact of disorder in the charge density wave state of Pd-intercalated ErTe$_3$ revealed by the electrodynamic response, Phys. Rev. Res. **5**, 033140 (2023).

[38] S. Xu, J. Gao, Z. Liu, K. Chen, P. Yang, S. Tian, C. Gong, J. Sun, M. Xue, J. Gouchi, X. Luo, Y. Sun, Y. Uwatoko, H. Lei, B. Wang, and J. Cheng, Effects of disorder and hydrostatic pressure on charge density wave and superconductivity in 2H$-$TaS$_2$, Phys. Rev. B **103**, 224509 (2021).

[39] S.-H. Baek, Y. Sur, K. H. Kim, M. Vojta, and B. Büchner, Interplay of charge density waves, disorder, and superconductivity in 2H-TaSe$_2$ elucidated by NMR, New J. Phys. **24**, 043008 (2022).

[40] A. Del Maestro, B. Rosenow, and S. Sachdev, From stripe to checkerboard ordering of charge-density waves on the square lattice in the presence of quenched disorder, Phys. Rev. B **74**, 024520 (2006).

[41] J. A. Robertson, S. A. Kivelson, E. Fradkin, A. C. Fang, and A. Kapitulnik, Distinguishing patterns of charge order: Stripes or checkerboards, Phys. Rev. B **74**, 134507 (2006).